

Investigating the probe-tip influence on imaging using scanning near-field optical microscopy

PANJI ACHMARI,^{1,2}  ARIF M. SIDDIQUEE,^{1,2,3}  GUANGYUAN SI,⁴
JIAO LIN,⁵ BRIAN ABBEY,^{1,2} AND SHANSHAN KOU^{1,2,*}

¹Department of Chemistry and Physics, La Trobe Institute for Molecular Science (LIMS), La Trobe University, Victoria 3086, Australia

²The Centre of Excellence for Advanced Molecular Imaging, La Trobe University, Victoria 3086, Australia

³Department of Electronic Science, Xiamen University, Xiamen 361005, China

⁴Melbourne Centre for Nanofabrication, Victorian Node of the Australian National Fabrication Facility, Victoria 3168, Australia

⁵School of Engineering, RMIT University, Victoria 3000, Australia

*s.kou@latrobe.edu.au

Abstract: The influence of the near-field probe-tip on a model sample consisting of one-dimensional apertures is investigated using scanning near-field optical microscopy (SNOM). We use finite-difference time-domain (FDTD) simulations combined with SNOM scans to show that the probe-tip has a rather profound effect on the shape of the measured transmission intensity profiles. By taking into account the near-field perturbations introduced by the probe, our newly developed FDTD model facilitates the quantitative analysis of SNOM data and provides new insights into near-surface, subwavelength optical interactions.

© 2021 Optical Society of America under the terms of the [OSA Open Access Publishing Agreement](#)

1. Introduction

Scanning near-field optical microscopy (SNOM) [1–3] is an intrinsically subwavelength resolution optical imaging technique [4,5]. SNOM imaging has been previously demonstrated for a broad range of applications, including the optical detection and characterization of single molecules [6–8], light localization in nanophotonic devices [9,10], plasmonics [11–13], and bioimaging [14,15]. Whilst the interactions between the probe-tip and the sample are still not well-understood, promising results have been obtained using SNOM by modifying either the probe-tip or sample environment [16]. SNOM uses a sharp optical probe incorporating a subwavelength aperture or a metallic tip, placed at a subwavelength distance from the sample surface, allowing for either localized optical near-field illumination or collection. The probe interacts with the non-propagating evanescent waves in the near-field regime, providing high spatial frequency information, which is often not accessible in the far-field. Whilst atomic force microscopy (AFM) is widely employed for investigating nanostructures, the additional near-field optical information provided by SNOM can be critical for unraveling the structure's functional relationships for a wide range of materials.

The near-field optical regime has a very interesting, yet complex behaviour. Scanning near-field optical microscopy studies involving the analysis of the light intensity profile within the local vicinity of the probe-tip have previously been performed [17]. In addition, there have been attempts to improve the quality of SNOM images by modifying the structure of the probe [18,19]. These previous studies suggest that the probe-tip plays a critical role in SNOM image formation. However, although advanced computational techniques such as the FDTD method [20] have facilitated the study of the near-field properties of various nanostructured materials and devices, to date, there have been very few studies focused on the influence of the SNOM probe-tip. The interface between the sample surface and the probe-tip is often overlooked when interpreting SNOM images due to the complexity of the necessary calculations involved when estimating the

evanescent field interactions between the two. However, the specific details of these interactions are known to play a critical role in SNOM image formation. Typically, modelling of SNOM image formation to investigate the near-field properties involves placing a two-dimensional (2D) 'detector' plane close to the sample surface to simulate the electric and magnetic fields [21–23]. This simple assumption of a 2D plane in place of the actual probe allows for fast and efficient simulations of the near-field properties of the sample. However, as we demonstrate here, the inclusion of a physical probe-tip in the calculation of the detected SNOM signal can lead to a wholesale modification of the resulting simulated intensity distribution. A previously published example of a simulation-only study of SNOM imaging [24] confirmed that the probe induces a strong scattering effect within the near-surface region of the sample which in turn has a significant effect on the resulting images. A much more recent study of the influence of the probe-tip on SNOM imaging was performed by looking at measurements of material boundaries using SNOM [25]. In this study, it was observed that including the probe-tip significantly modified the signal measured from the interface between two materials. An analysis of the local interaction between the probe-tip and the sample has previously been studied by investigating the near-field interference pattern produced by surface plasmons generated by a square arrangement of slit apertures [26].

In the present work, the idea of incorporating the probe-tip into FDTD simulations to understand and interpret SNOM imaging is further developed. To verify the results of these simulations experimentally, single- and double-slit apertures are used. These samples exhibit significantly more complex behaviour than discrete boundaries [25] and, as we show by varying the aperture width and separation, the relative influence of the probe-tip is size-scale dependent. The use of apertures allows us to examine the effect of the probe for a range of different sample parameters and, as a consequence, develop a more accurate model for aperture-type SNOM. In addition, since the one-dimensional apertures have a well-defined length scale which can be varied at the nanoscale and can be readily fabricated with very high quality, they have also been previously imaged in the published literature [27,28]. Simulating these apertures using the FDTD is also computationally straightforward and as they are one-dimensional, variations along only one axis need to be considered.

2. Experimental and simulation setup

Figures 1(a-b) show the schematic of the experimental set-up used in this study and the zoomed-in layout of the sample and the SNOM probe, which was used for modelling the experiment in the simulation. The near-field imaging was performed using the NTEGRA Solaris SNOM supplied by NT-MDT. The SNOM was operated in collection mode, i.e. the probe collects the near-field signal from the sample under far-field illumination from the objective lens. A spatially filtered laser beam, with $\lambda = 640$ nm, passes through a beam splitter (see Fig. 1(a)) and the outgoing beam from the beam splitter enters the objective lens (10x/NA 0.30), illuminating the sample which sits on a microscope stage. The focal plane, with beam waist = $80\ \mu\text{m}$, is between 5-10 mm from the sample surface, resulting in a beam size of between $300\ \mu\text{m}$ to $600\ \mu\text{m}$ on the sample surface. The light collected by the optical probe is guided through an optical fiber to a photo-multiplier tube (PMT) detector. The reflected signal from the sample enters the beam splitter and is detected by the camera.

Imaging was performed in a constant-gap mode, and the results were checked against measurements performed in a constant-height mode to eliminate the possibility of SNOM imaging artifacts [29–31]. The final intensity line profiles across the nanoslits were calculated by taking average from 100 lineouts spaced evenly along the long axis of the slit. The averaging was performed to increase the signal-to-noise ratio and to suppress the effect of any imperfections or irregularities in the sample.

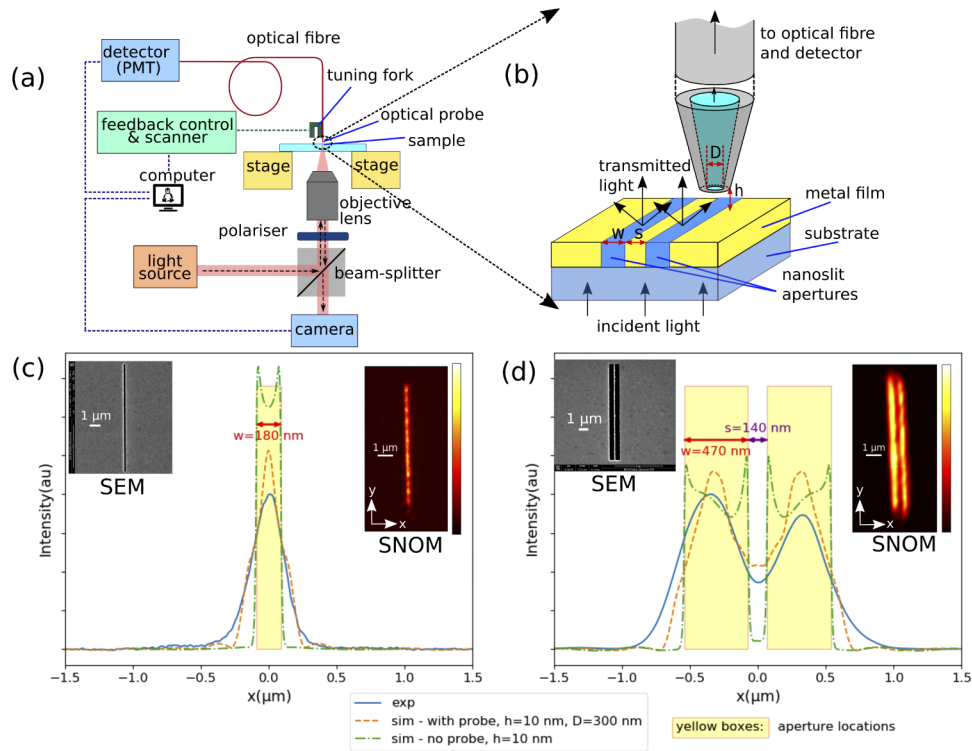


Fig. 1. (a) The experimental layout for SNOM imaging and (b) zoomed-in region of the SNOM probe and the sample. (c-d) Example comparisons of FDTD simulation with (dashed orange line) and without (dashed green line) the probe-tip incorporated. The corresponding experimental data is also shown (solid blue line). The simulated probe-tip was assumed to be at a height (h) of 10 nm from the surface and the simulated probe aperture diameter (D) was 300 nm. Results are presented for (c) a single-slit ($w = 180$ nm) and (d) a double-slit pair ($w = 470$ nm, $s = 140$ nm). The corresponding SEM and SNOM images are shown in the top left-hand and right-hand corners respectively of (c) and (d).

Full-wave FDTD simulations were carried out using the commercially available Lumerical software. The simulations were performed to model the collection of light by the probe as shown in Fig. 1(b). The simulation included an optical probe, formed by concentric truncated cones with a full-cone angle of 20° . The probe was modelled as being made from glass core (with $n = 1.5$), with Cr (20 nm)/Al (70 nm) cladding, as specified by the manufacturer. The sample was modelled as being illuminated by a Gaussian beam source incident from the substrate side. The light transmitted through the nanoslit apertures in a gold film and the resulting transmitted optical power was recorded. Both the experiment and simulation used s-polarized light where the electric field was aligned perpendicularly with respect to the nanoslit aperture. We investigated the variation in the aperture size of the SNOM probe-tip, keeping the metal coating thickness and the cone angle constant along the length of the probe. The upper portion of the probe extended out across the simulation boundary. A two-dimensional (2D) field monitor was placed at the tip of the probe to record the electromagnetic signal collected by the probe. A non-uniform mesh was used in the FDTD simulations, which had a resolution ranging between 5 nm to 40 nm. Close to the slit apertures and in the vicinity of the probe-tip, a 5 nm mesh was used, whilst a 40 nm mesh was applied in the regions with a slowly varying field gradient, far from any structures/

objects. Between the 5 nm and 40 nm meshes, there was a continuous graduation in the mesh resolution to avoid any discontinuities in the simulations.

The time-averaged transmitted power P into the optical probe was calculated by integrating the Poynting vector over the probe-tip area A ,

$$P = \int_A \text{Re}(\vec{S}) \cdot d\vec{A}, \quad (1)$$

where $\vec{S} = \frac{1}{2}(\vec{E} \times \vec{H}^*)$, is the complex Poynting vector. This calculation assumed that the light propagating into the probe is similar to the wave propagation in a waveguide [32]. The simulation was repeated for every (x, y) position of the probe to form a complete image, mirroring the manner in which SNOM data was collected during an experiment. Due to the symmetry of the nanoslits, only the variation in the x -direction, perpendicular to the long axis of the slit apertures, was calculated (see insets Fig. 1(c-d)). The simulated probe-tip was moved at a constant-height with respect to the sample. For conventional FDTD simulations, the 2D plane monitor was placed at a fixed distance from the sample to record the near-field intensity profile. In order to be able to directly compare the two different simulation approaches (i.e. with and without the probe-tip) to the experimental SNOM data, each dataset was normalized with respect to the total energy (total area under the intensity curve) so that they were correctly scaled with respect to one another. The normalization of the intensity profiles involved calculating the total area underneath each line profile via integration with respect to the distance (x) . Each profile was then multiplied by a constant value such that the area in each case summed to unity. In this way, we ensured that the total energy associated with each individual intensity plot was normalised to the same value.

Fitting of the intensity profiles in order to determine the FWHM and peak-to-peak distance was carried out using the pseudo-Voigt function (f_V) which is a linear combination of Lorentzian (f_L) and Gaussian (f_G) functions, i.e.:

$$f_V = \eta f_L + (1 - \eta) f_G = \eta \frac{A}{1 + \left(\frac{x-x_0}{\gamma}\right)^2} + (1 - \eta) A \exp\left(-\frac{(x-x_0)^2}{2\sigma^2}\right) \quad (2)$$

where η is the linear combination factor with $0 \leq \eta \leq 1$, A is the peak amplitude, and x_0 specifies the location of the peak maximum intensity value for the x -component of the transmission profile. The values of γ and σ are related to each other via FWHM, which is given by:

$$\text{FWHM} = 2\gamma = (2\sqrt{2 \ln 2})\sigma. \quad (3)$$

The optimum values for η , A , x_0 , and FWHM were calculated via a non-linear least-squares fit to the data.

3. Results and discussion

Single slit apertures of length $10 \mu\text{m}$ and width (w) between 150 nm and 410 nm were fabricated in a 200 nm-thick gold film. In addition, double slit apertures were also fabricated, these had the same length ($10 \mu\text{m}$) as the single slits but had a slightly wider range of aperture widths ($w = 410 \text{ nm to } 480 \text{ nm}$) as well as being fabricated in a slightly thinner 120 nm gold film. Note that the reason for the thinner film for the double slits was to enable the fabrication of two adjacent features with very small separation using focused ion beam (FIB) technique. In the case of both 120 nm and 200 nm thick gold films, the optical transmission should be negligible. For the double slit samples, the slit separation (s) was varied between 80 nm and 230 nm. The structures were separated from each other by a minimum of $20 \mu\text{m}$, to ensure that there was no interference between individual samples during the SNOM scan. Table 1 shows the structures considered in this study.

Table 1. The dimensions of the slit apertures (width w and separation s shown) as confirmed by scanning electron microscopy (SEM).

No.	single-slit	double-slit	
	w (nm)	w (nm)	s (nm)
1	150	410	80
2	180	470	140
3	410	480	230

Example comparisons between the experimentally acquired data and the numerically calculated data obtained from FDTD simulations are shown in Figs. 1(c-d). The corresponding SEM and SNOM images of the slit apertures are shown in the inset. The examples are presented both for a single-slit aperture (Fig. 1(c)) and double-slit aperture pair (Fig. 1(d)). The intensity line profiles from the experiment were obtained by averaging the line profiles perpendicular to the long axis of the slits. The data were normalized so that the results from the different approaches could be directly compared as described in the previous section. In order to investigate the effect of wavelength on the relative influence of the probe-tip interaction we repeated the simulations over a range of different wavelengths from 500 nm to 640 nm (see Supplement 1). We observe, based on the simulated intensity profiles, that although there are small differences, any variations are, in general, minor and are consistent with the results obtained at 640 nm.

The experimental results (solid-blue lines) confirmed intensity peaks corresponding to the slit locations (Fig. 1(c-d)), one clear peak was observed for the single-slit and two distinct peaks were recorded for the double-slit apertures. The resulting line profiles may be approximated using Gaussian or Lorentzian functions. A linear combination of these functions (pseudo-Voigt function) were used to fit the experimental data and to determine a value for the full-width at half-maximum (FWHM) of the signal from the slits. The position of the slits in Figs. 1(c) and 1(d) indicated by the yellow shading correspond to the parameters shown in Table 1. We note that although qualitatively the positions of the measured intensity peaks match those expected from the SEM images, there is a slight asymmetry between them, which we attribute to imperfections in the fabrication (e.g. material re-deposited at the edge of the slit).

The intensity profiles obtained from FDTD simulations with and without the probe were overlaid on top of the experimental line profiles in Figs. 1(c) and (d) for comparison. The effect of varying the probe aperture diameter (D) and probe-tip-sample separation (h) was also investigated, as discussed in the second half of this paper. For FDTD simulations without the probe, a simple 2D flat monitor set at $h = 10$ nm, was used to record the near-surface intensity distribution. If the probe-tip is ignored, the FDTD simulations produced 'top-hat' like distributions with oscillations in the intensity at the edges of the slits and a very rapid decay at the intensity tails. The slit apertures used in our study are isolated nanostructures and when illuminated, these structures generate both surface plasmon polaritons (SPPs) and localized surface plasmons (LSPs) at the metal-dielectric interface of the thin film. However, it is the LSPs which are the dominant cause of the observed 'fine-structure' oscillatory peaks at the edges of the slits, even though the overall profile shape is a result from the combined effect of both SPPs and LSPs [33,34]. The simulated intensity profiles without the probe-tip, which is the approach typically employed in literature, clearly do not match the details of the actual measured SNOM images. When the flat plane monitor is replaced by a numerically modelled SNOM probe-tip, there is a marked change in the simulated SNOM profile. The calculated profiles become 'rounder' with a much more gradual decay of the intensity profile outside of the expected area of the nanoslit apertures. It is clear from a systematic comparison of experimental data to those with simulated ones that the presence of the probe-tip has a rather profound influence on the measured profile. This agrees with the prediction of the recent study [25] in which the asymmetries in the measured SNOM profiles of

material boundaries could only be recreated in simulations by incorporating the probe-tip. The use of slit apertures in the present study allows us to further investigate this effect as a function of the aperture dimensions and (subwavelength) aperture separation, in which the two slit apertures can no longer be considered as independent features.

In the literature, there have been reports of enhancement or modification of the near-field signal due to local inhomogeneities in both the probe-tip and sample [30]. For example, enhanced light transmission through the probe aperture was demonstrated [19] by incorporating a single groove inside the tip with a resulting improvement in spatial resolution. Such approaches could also benefit nanospectroscopy studies using near-field Raman spectroscopy where signal strength is currently a major challenge for sample characterization [35]. In order to gain an overall understanding of the effect of the tip, our model assumed the ideal case of a perfectly round probe-tip aperture and smooth slit edges. The measured signal therefore assumed that all incident light travels through the waveguide (probe-tip aperture) and optical fiber without any scattering/losses prior to being detected by the photomultiplier tube (PMT). We note that the probe-tip aperture used in this study has a diameter of $D = 125 \pm 25$ nm (as specified by the manufacturer – TipsNano). This is smaller than the 'effective' aperture size of 300 nm obtained from fitting of the experimental SNOM profiles. The reason that the experimentally determined aperture diameter is larger than the physical size specified by the manufacturer is likely due to the effect of probe asperities and inhomogeneities as well as scattered light reaching the PMT (e.g. from the edges of the slits or the probe itself [24]). These effects broaden the size of the 'ideal probe' which was assumed in our FDTD simulations. The quality of fit between the simulated and experimental data indicates that these effects may, to a first-order approximation, be accounted for by increasing the effective size of the probe used in the model. The combination of FDTD simulations and experimental measurements of the slit apertures thus enables us to investigate the relative impact of the probe-tip in aperture-type SNOM image formation.

To investigate the effect of the probe-tip aperture on the measured SNOM intensity, FDTD simulations (with and without the probe included) were conducted for a range of different parameters. Some example results are in Fig. 2. Figures 2(a-c) show the simulation results for a single-slit aperture ($w = 180$ nm), and Figs. 2(d-f) show the simulation results for double-slit apertures ($w = 480$ nm and $s = 140$ nm) without (a,d) and with (b,c,e,f) the probe included. In the simulation without the probe (first column in Fig. 2), the line profiles become steadily more blurred with the increasing distance between the plane detector and the sample surface. For example, we observe that for $h > 50$ nm, it is no longer possible to resolve the double slits, this is consistent with the fact that the near-field resolution enhancement from the SNOM quickly degrades as a function of detector distance.

The effect of incorporating the probe-tip in the simulation is illustrated in the second and third columns of Fig. 2. In Figs. 2(b,e), D is varied from 100 nm and 500 nm, with the probe distance fixed at $h = 10$ nm for both the single-slit and double-slit apertures. By including the probe-tip in the FDTD simulations, a number of very significant differences in the simulated intensity profiles were observed. The most obvious one is the lack of any sharp features/ variations in the calculated intensities when including the probe. For example, even for $h = 10$ nm, the simulations with the probe do not indicate a sharp edge of the apertures, but rather a more gentle decay of the intensity. Qualitatively, these features match very well with the experimental SNOM data (as shown in Fig. 1). This is in contrast to simulations without the probe-tip which predicted a number of features that were not present in the experimental data. Interestingly, the simulations with the probe included showed that starting from a certain minimum probe size ($D = 300$ nm), the double slits can still be resolved, even for $h = 100$ nm (Fig. 2(f)). In fact, we generally observe that provided the probe-tip remains within the near-field region of the sample, the probe aperture size has a more significant impact on the calculated intensity profiles than the distance from the sample surface. It has previously been established that the aperture diameter of the probe-tip may

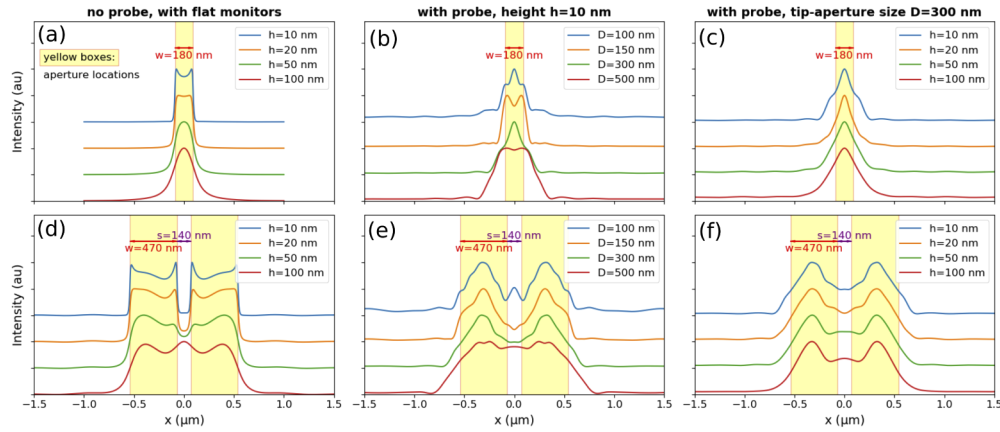


Fig. 2. FDTD simulations for (a-c) a single-slit aperture with the width $w = 180$ nm and (d-f) double-slit apertures with the width $w = 470$ nm and separation $s = 140$ nm. Data were normalized with respect to the maximum peak height and are offset vertically with respect to each other for ease of comparison. (a,d) Simulation without the probe using a 2D flat monitor for $h = 10$ nm, 20 nm, 50 nm and 100 nm. (b,e) Simulation with the probe having $D = 100$ nm, 150 nm, 300 nm and 500 nm. Note that for $D = 500$ nm the double slits are no longer resolved. (c,f) Simulation with the probe included for $D = 300$ nm and $h = 10$ nm, 20 nm, 50 nm and 100 nm.

have a significant influence on the measured near-field component in SNOM imaging [25,26]. Hence, our findings are in agreement with the published literature. It is important to note that in simulations presented in this paper, the parameters (D and h) were chosen to be consistent with the experimental SNOM measurements.

Figure 3 compares experimental data collected using SNOM from single and double slits, with FDTD simulations carried out with and without the probe-tip included. For the single slit aperture, the results for $w = 150$ nm and 410 nm are shown. For the double slits, the slit parameter $s = 230$ nm and 80 nm, corresponding to a $w = 480$ nm and 410 nm respectively, have been chosen. The full-widths at half-maximum (FWHMs) for single-slit apertures, which should be approximately equal to w , along with the SEM values for the slit widths are summarized in Table 2. Focusing on comparing the experimental SEM data to the results of the SNOM scan, we observed that for the widest aperture, the SEM and SNOM results were comparable (within 10 nm). As the aperture size decreases, the relative discrepancy between the SEM and SNOM results increases. This is due to the higher spatial resolution achievable with SEM (8 nm) compared to the spatial resolution of SNOM, which was estimated from the analysis of edge profile scans to be $178 \text{ nm} \pm 14 \text{ nm}$ [36].

Table 2. Summary of the differences between experimental (exp) and FDTD simulation (sim) results for single slit apertures, comparing FWHM obtained for the slits.

SEM		FWHM (nm)	
w (nm)	exp		sim
150	265		255
180	275		250
410	400		335

The effect of the finite optical resolution results in blurring of the slit profiles, making the slits look wider than as seen in SEM images when their dimensions are comparable to the resolution

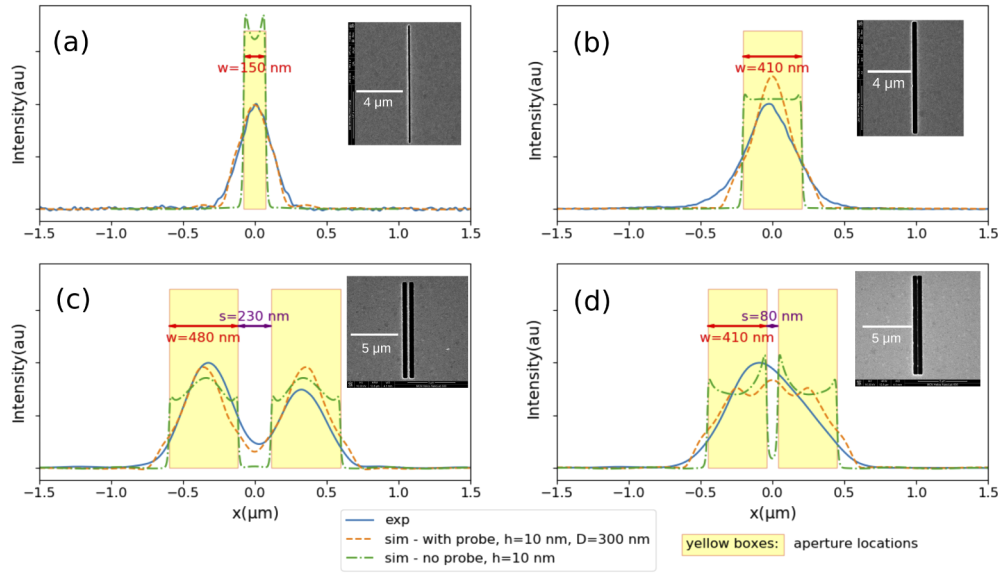


Fig. 3. The comparison between experimental and FDTD simulation results for single-slit apertures with (a) $w = 150$ nm and (b) $w = 410$ nm, and for double-slit apertures with (c) $w = 480$ nm and $s = 230$ nm, and (d) $w = 410$ nm and $s = 80$ nm. The experimental results are consistent with the simulation results with the probe.

of the SNOM. Consistent with the results shown in Fig. 1, when the FDTD parameters were set to $h = 10$ nm and $D = 300$ nm, the main features of the experimental single slit data were reproduced when the probe-tip was included in the simulations. By contrast, with no probe and just a flat plane detector, the resulting calculated intensity profiles differed from the actual experimental SNOM data.

A comparison of the experimental and FDTD simulated line profiles for the double slits is shown in Fig. 3(c-d). We note that for the experimental SNOM double slit data there is a small asymmetry in the measured intensity profiles. This is because some of the removed material re-attaches within the area of the first slit when the second slit is fabricated. This means that the optical transmission measured by SNOM through the slits is slightly different. We observed that in the SNOM experiment for the double slits with $s = 80$ nm, the two slits could not be resolved, which is consistent with the estimated spatial resolution of the SNOM. As was the case with the single slit data, the FDTD simulations with the probe were able to reproduce the experimental SNOM image more accurately. The summary of the calculated FWHMs for both experimental and simulation data are shown in Table 3. In addition, the peak-to-peak distance in the intensity profile was also calculated, which was used to show comparable distances to the centre-to-centre values measured from SEM images.

To further explore the quantitative predictions from the FDTD model, we used the parameters (D and h) determined from the fitting the experimental data in Fig. 1 to predict unknown slit size, and compared the results to those obtained from the SEM. Figure 4 presents a summary of the results for the single slit widths using the FDTD model. These slit values were obtained by iteratively updating w in order to minimize the error metric between the simulated and experimental SNOM data. The simulated results for w , ranging from 100 nm to 300 nm, are shown for both coarse and fine increments of w . The intensity line profile from the experiment (I_{exp}) is overlaid with each calculated line profile from the simulation (I_{sim}). The difference between them is determined from the error metric, i.e. $e_{abs} = |I_{exp} - I_{sim}|$. Two different experimental results with different

Table 3. Summary of the differences between experimental and FDTD simulation results for double slit apertures, comparing FWHM, and peak-to-peak distance. Center-to-center distances between the slits obtained from SEM images are included. Note that data for $s = 80$ nm is omitted as the peaks could not be resolved (see Fig. 3(d)).

SEM			FWHM (nm)			peak-to-peak (nm)	
w (nm)	s (nm)	center-to-center (nm)	exp, left	exp, right	sim	exp	sim
470	140	610	495	455	420	685	630
480	230	710	390	375	370	655	705

widths are examined here. For $w_{SEM} = 150$ nm (Fig. 4(a)), iteratively updating w in (initially) coarse and then fine steps yielded a minimum error at $w_{sim} = 160$ nm. The same process was repeated for $w_{SEM} = 180$ nm (Fig. 4(b)) with the minimum error found at $w_{sim} = 180$ nm. These

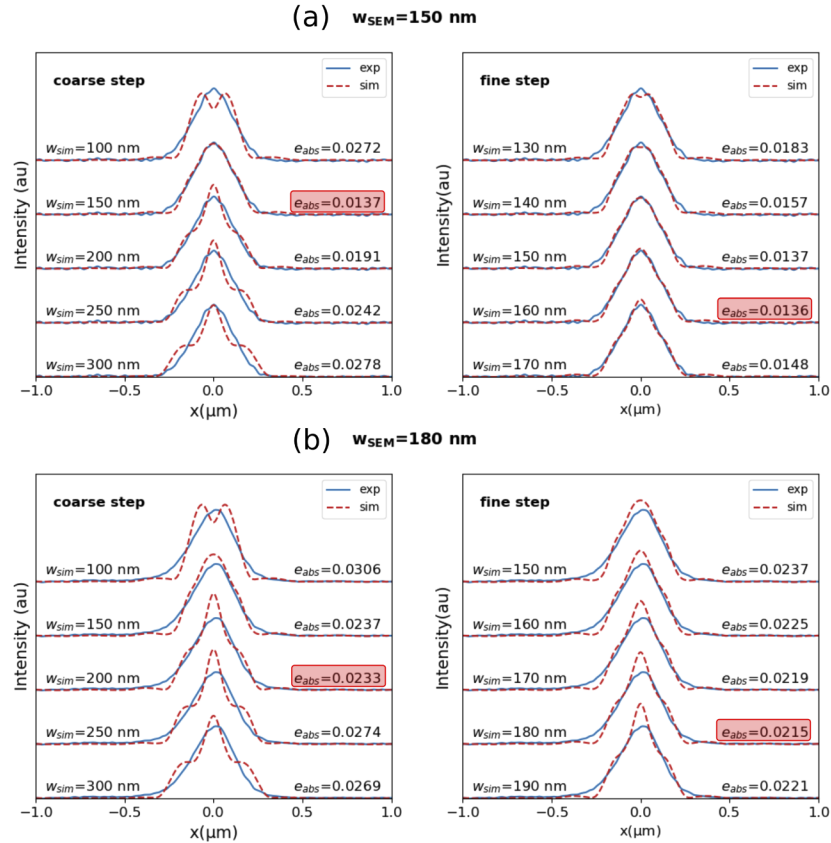


Fig. 4. Determining (estimating) the actual width of the slit by finding the minimum of the absolute error e_{abs} between the experimental (exp) and simulation (sim) intensity profiles (achieved for probe parameters $D = 300$ nm and $h = 10$ nm), for the slits with the width (obtained from SEM images) of (a) $w_{SEM} = 150$ nm and (b) $w_{SEM} = 180$ nm. The first column shows width iteration with rough step of 50 nm, and the second column shows the finer step of 10 nm, with the minimum error annotated in red. The minimum errors were found for the simulated widths $w_{sim} = 160$ nm and $w_{sim} = 180$ nm, respectively. The profiles are shifted upward for clarity.

matching results demonstrate that our FDTD model based on the inclusion of a probe-tip into SNOM imaging is a valid and accurate approach to represent realistic SNOM imaging conditions.

4. Conclusions

We have shown that the optical probe-tip has a critical influence on the resulting SNOM images. Using single- and double-slit aperture samples fabricated in gold film with FIB, we are able to demonstrate that the inclusion of a simplified probe-tip in FDTD simulations leads to a dramatic improvement in representing true intensity profiles of our model sample of single- and double-slit apertures. The widely employed 2D plane detector without considering the effect of the probe failed to reproduce valid intensity profiles for several cases we demonstrated here. Furthermore, by accounting for the near-field modification induced by the probe-tip, our results indicate that the key properties (e.g. intensity profiles and FWHM) and feature sizes (widths w) associated with the single-slit aperture samples may be accurately predicted. The FDTD simulation model that we have described and developed here can be used to explore and investigate any changes or modification to the SNOM probe-tip. Modification or functionalization of the probe-tip is an active topic of research in atomic force microscopy (AFM) and scanning tunnelling microscopy (STM) [37–40], as well as in SNOM [16,19,41]. These types of modifications often involve altering the interaction force between the probe-tip and the sample to improve the sensitivity and/or resolution of the image. For example, modification of the probe-tip via the introduction of subwavelength structures such as grooves [19], has been shown to potentially improve the spatial resolution by a factor of 2 and enhance the transmitted field by around two orders of magnitude. The simulation approach we present here could be used to understand the effect of modifying the interaction between the probe and sample through functionalization as well as better predict the optical characteristics of conventional SNOM imaging.

Acknowledgment. P.A. acknowledges the James T. Riady Research Scholarship. S.S.K. acknowledges the support from La Trobe University's Research Infrastructure Grant for purchasing the SNOM. This work was performed in part at the Melbourne Centre for Nanofabrication (MCN) in the Victorian Node of the Australian National Fabrication Facility (ANFF).

Disclosures. The authors declare no conflicts of interest.

Supplemental document. See [Supplement 1](#) for supporting content.

References

1. D. Pohl, U. C. Fischer, and U. Dürig, "Scanning near-field optical microscopy (SNOM)," *J. Microsc.* **152**(3), 853–861 (1988).
2. A. Rasmussen and V. Deckert, "New dimension in nano-imaging: breaking through the diffraction limit with scanning near-field optical microscopy," *Anal. Bioanal. Chem.* **381**(1), 165–172 (2005).
3. A. Lereu, A. Passian, and P. Dumas, "Near field optical microscopy: a brief review," *Int. J. Nanotechnol.* **9**(3/4/5/6/7), 488 (2012).
4. R. C. Dunn, "Near-field scanning optical microscopy," *Chem. Rev.* **99**(10), 2891–2928 (1999).
5. B. Hecht, B. Sick, U. P. Wild, V. Deckert, R. Zenobi, O. J. Martin, and D. W. Pohl, "Scanning near-field optical microscopy with aperture probes: Fundamentals and applications," *J. Chem. Phys.* **112**(18), 7761–7774 (2000).
6. A. J. Meixner, D. Zeisel, A. M. Bopp, and G. Tarrach, "Super-resolution imaging and detection of fluorescence from single molecules by scanning near-field optical microscopy," *Opt. Eng.* **34**(8), 2324–2333 (1995).
7. H. G. Frey, S. Witt, K. Felderer, and R. Guckenberger, "High-resolution imaging of single fluorescent molecules with the optical near-field of a metal tip," *Phys. Rev. Lett.* **93**(20), 200801 (2004).
8. J. Kim, T. Ohtani, and H. Muramatsu, "25 nm resolution single molecular fluorescence imaging by scanning near-field optical/atomic force microscopy," *Surf. Sci.* **549**(3), 273–280 (2004).
9. B. J. Bohn, M. Schnell, M. A. Kats, F. Aieta, R. Hillenbrand, and F. Capasso, "Near-field imaging of phased array metasurfaces," *Nano Lett.* **15**(6), 3851–3858 (2015).
10. M. Schnell, P. Sarriugarte, T. Neuman, A. Khanikaev, G. Shvets, J. Aizpurua, and R. Hillenbrand, "Real-space mapping of the chiral near-field distributions in spiral antennas and planar metasurfaces," *Nano Lett.* **16**(1), 663–670 (2016).
11. S. Kawata, Y. Inouye, and P. Verma, "Plasmonics for near-field nano-imaging and superlensing," *Nat. Photonics* **3**(7), 388–394 (2009).

12. M. Schnell, A. Garcia-Etxarri, A. Huber, K. Crozier, J. Aizpurua, and R. Hillenbrand, "Controlling the near-field oscillations of loaded plasmonic nanoantennas," *Nat. Photonics* **3**(5), 287–291 (2009).
13. K. Imura, T. Nagahara, and H. Okamoto, "Imaging of surface plasmon and ultrafast dynamics in gold nanorods by near-field microscopy," *J. Phys. Chem. B* **108**(42), 16344–16347 (2004).
14. T. Yoshino, S. Sugiyama, S. Hagiwara, T. Ushiki, and T. Ohtani, "Simultaneous collection of topographic and fluorescent images of barley chromosomes by scanning near-field optical/atomic force microscopy," *J. Electron Microsc.* **51**(3), 199–203 (2002).
15. A. Rothery, J. Gorelik, A. Bruckbauer, W. Yu, Y. Korchev, and D. Klenerman, "A novel light source for SICM–SNOM of living cells," *J. Microsc.* **209**(2), 94–101 (2003).
16. A. F. Raigoza, J. W. Dugger, and L. J. Webb, "Recent advances and current challenges in scanning probe microscopy of biomolecular surfaces and interfaces," *ACS Appl. Mater. Interfaces* **5**(19), 9249–9261 (2013).
17. A. A. Kuchmizhak, Y. N. Kulchin, O. B. Vitrik, A. G. Savchuk, S. V. Makarov, S. I. Kudryashov, and A. A. Ionin, "Optical apertureless fiber microprobe for surface laser modification of metal films with sub-100 nm resolution," *Opt. Commun.* **308**, 125–129 (2013).
18. J. T. Krug, E. J. Sánchez, and X. S. Xie, "Design of near-field optical probes with optimal field enhancement by finite difference time domain electromagnetic simulation," *J. Chem. Phys.* **116**(24), 10895–10901 (2002).
19. T. Antosiewicz and T. Szoplik, "Corrugated SNOM probe with enhanced energy throughput," *Opto-Electron. Rev.* **16**(4), 451–457 (2008).
20. A. Taflov and S. C. Hagness, *Computational electrodynamics: the finite-difference time-domain method* (Artech house, 2005).
21. E. X. Jin and X. Xu, "Finite-difference time-domain studies on optical transmission through planar nano-apertures in a metal film," *Jpn. J. Appl. Phys.* **43**(1), 407–417 (2004).
22. A. Goncharenko, H.-C. Chang, and J.-K. Wang, "Electric near-field enhancing properties of a finite-size metal conical nano-tip," *Ultramicroscopy* **107**(2-3), 151–157 (2007).
23. J. Abed, F. Alexander, I. Taha, N. Rajput, C. Aubry, and M. Jouiad, "Investigation of broadband surface plasmon resonance of dewetted Au structures on TiO₂ by aperture-probe SNOM and FDTD simulations," *Plasmonics* **14**(1), 205–218 (2019).
24. H. Furukawa and S. Kawata, "Analysis of image formation in a near-field scanning optical microscope: effects of multiple scattering," *Opt. Commun.* **132**(1-2), 170–178 (1996).
25. S. Mastel, A. A. Govyadinov, C. Maissen, A. Chuvilin, A. Berger, and R. Hillenbrand, "Understanding the image contrast of material boundaries in IR nanoscopy reaching 5 nm spatial resolution," *ACS Photonics* **5**(8), 3372–3378 (2018).
26. P. Dvořák, Z. Édes, M. Kvapil, T. Šamořil, F. Ligmajer, M. Hrtoň, R. Kalousek, V. Křápek, P. Dub, J. Spousta, P. Varga, and T. Šikola, "Imaging of near-field interference patterns by aperture-type snom—influence of illumination wavelength and polarization state," *Opt. Express* **25**(14), 16560–16573 (2017).
27. Y. Xie, A. R. Zakharian, J. V. Moloney, and M. Mansuripur, "Transmission of light through slit apertures in metallic films," *Opt. Express* **12**(25), 6106–6121 (2004).
28. Y. Pang, C. Genet, and T. Ebbesen, "Optical transmission through subwavelength slit apertures in metallic films," *Opt. Commun.* **280**(1), 10–15 (2007).
29. S. I. Bozhevolnyi, "Topographical artifacts and optical resolution in near-field optical microscopy," *J. Opt. Soc. Am. B* **14**(9), 2254–2259 (1997).
30. G. Kaupp, A. Herrmann, and M. Haak, "Artifacts in scanning near-field optical microscopy (SNOM) due to deficient tips," *J. Phys. Org. Chem.* **12**(11), 797–807 (1999).
31. A. M. Siddiquee, I. Y. Hasan, S. Wei, D. Langley, E. Balaur, C. Liu, J. Lin, B. Abbey, A. Mechler, and S. Kou, "Visualization and measurement of the local absorption coefficients of single bilayer phospholipid membranes using scanning near-field optical microscopy," *Biomed. Opt. Express* **10**(12), 6569–6579 (2019).
32. J. D. Jackson, "Classical electrodynamics," (1999).
33. S. A. Maier, *Plasmonics: fundamentals and applications* (Springer Science & Business Media, 2007).
34. J.-Y. Laluet, A. Drezet, C. Genet, and T. Ebbesen, "Generation of surface plasmons at single subwavelength slits: from slit to ridge plasmon," *New J. Phys.* **10**(10), 105014 (2008).
35. W. Zhang, Z. Fang, and X. Zhu, "Near-field raman spectroscopy with aperture tips," *Chem. Rev.* **117**(7), 5095–5109 (2017).
36. P. Dean, O. Mitrofanov, J. Keeley, I. Kundu, L. Li, E. H. Linfield, and A. Giles Davies, "Apertureless near-field terahertz imaging using the self-mixing effect in a quantum cascade laser," *Appl. Phys. Lett.* **108**(9), 091113 (2016).
37. R. Barattin and N. Voyer, "Chemical modifications of AFM tips for the study of molecular recognition events," *Chem. Commun.* **13**, 1513–1532 (2008).
38. C. Volcke, R. P. Gandhiraman, V. Gubala, C. Doyle, G. Fonder, P. A. Thiry, A. A. Cafolla, B. James, and D. E. Williams, "Plasma functionalization of AFM tips for measurement of chemical interactions," *J. Colloid Interface Sci.* **348**(2), 322–328 (2010).
39. V. Giliberti, E. Sakat, M. Bollani, M. V. Altoe, M. Melli, A. Weber-Bargioni, L. Baldassarre, M. Celebrano, J. Frigerio, G. Isella, S. Cabrini, and M. Ortolani, "Functionalization of scanning probe tips with epitaxial semiconductor layers," *Small Methods* **1**(3), 1600033 (2017).

40. B. Konoplev, O. Ageev, V. Smirnov, A. Kolomiitsev, and N. Serbu, "Probe modification for scanning-probe microscopy by the focused ion beam method," *Russ. Microelectron.* **41**(1), 41–50 (2012).
41. E. G. Bortchagovsky, U. C. Fischer, and T. Schmid, "Possibilities of functionalized probes in optical near-field microscopy," *Phys. Scr.* **T162**, 014005 (2014).